The visible spectrum of zirconium dioxide, ZrO_2

Anh Le, Timothy C. Steimle', Varun Gupta, Corey A. Rice, John P. Maier, Sheng H. Lin, and Chih-Kai Lin

Citation: The Journal of Chemical Physics **135**, 104303 (2011); doi: 10.1063/1.3632053
View online: http://dx.doi.org/10.1063/1.3632053
View Table of Contents: http://aip.scitation.org/toc/jcp/135/10
Published by the American Institute of Physics

The visible spectrum of zirconium dioxide, ZrO_2

Anh Le,[1] Timothy C. Steimle,[1,a)] Varun Gupta,[2] Corey A. Rice,[2] John P. Maier,[2] Sheng H. Lin,[3] and Chih-Kai Lin[3]
[1]*Department of Chemistry and Biochemistry, Arizona State University, Tempe, Arizona 85287-1604, USA*
[2]*Department of Chemistry, University of Basel, Basel, Switzerland*
[3]*Department of Applied Chemistry, National Chiao Tung University, Hsinchu, Taiwan*

(Received 8 July 2011; accepted 12 August 2011; published online 8 September 2011)

The electronic spectrum of a cold molecular beam of zirconium dioxide, ZrO_2, has been investigated using laser induced fluorescence (LIF) in the region from 17 000 cm^{-1} to 18 800 cm^{-1} and by mass-resolved resonance enhanced multi-photon ionization (REMPI) spectroscopy from 17 000 cm^{-1}–21 000 cm^{-1}. The LIF and REMPI spectra are assigned to progressions in the $\tilde{A}^1B_2(\nu_1, \nu_2, \nu_3) \leftarrow \tilde{X}^1A_1(0, 0, 0)$ transitions. Dispersed fluorescence from 13 bands was recorded and analyzed to produce harmonic vibrational parameters for the $\tilde{X}^1A_1$ state of $\omega_1 = 898(1)$ cm^{-1}, $\omega_2 = 287(2)$ cm^{-1}, and $\omega_3 = 808(3)$ cm^{-1}. The observed transition frequencies of 45 bands in the LIF and REMPI spectra produce origin and harmonic vibrational parameters for the $\tilde{A}^1B_2$ state of $T_e = 16\,307(8)$ cm^{-1}, $\omega_1 = 819(3)$ cm^{-1}, $\omega_2 = 149(3)$ cm^{-1}, and $\omega_3 = 518(4)$ cm^{-1}. The spectra were modeled using a normal coordinate analysis and Franck-Condon factor predictions. The structures, harmonic vibrational frequencies, and the potential energies as a function of bending angle for the $\tilde{A}^1B_2$ and $\tilde{X}^1A_1$ states are predicted using time-dependent density functional theory, complete active space self-consistent field, and related first-principle calculations. A comparison with isovalent TiO_2 is made.
 [doi:10.1063/1.3632053]

I. INTRODUCTION

The metal-oxygen bond is of relevance in numerous chemical and biological processes. Insight into these phenomena can be effectively garnered by studying isolated gas-phase metal oxides for which both experimentation and theory can be quantitative. A perusal of the recent review[1] reveals that spectroscopic and theoretical studies of transition metal dioxides are sparse in comparison to metal monoxides. Given the technological importance of titania, it is understandable that gas-phase TiO_2 is amongst the most thoroughly studied. Studies of isovalent ZrO_2, the subject of the present investigation, are fewer. Theoretical studies for both TiO_2 and ZrO_2 greatly outnumber experimental studies due to difficulties of generation and detection of these ephemeral molecules. The dioxides can have one of three isomeric forms; (a) the inserted form, similar to TiO_2, with a large apex angle, (b) a "T-Shaped" form with a small apex angle and an O–O distance close to that of O_2, and (c) a M–O–O superoxide form. Sometime ago, an electrostatic deflection experiment determined that that ground state ZrO_2 had a permanent electric dipole moment,[2] thus ruling out the linear OZrO structure. The infrared absorption spectra of an argon matrix isolated sample was recorded,[3] and the observed isotopic shifts determined that the ground state structure is the inserted C_{2v} form. The $\nu_1(a_1)$ symmetric stretching frequency, ω_1, and the $\nu_3(b_2)$ antisymmetric stretching frequency, ω_3, were inferred to be 884.3 cm^{-1} and 818.0 cm^{-1}, respectively. The isotopic dependence of ω_3 was used to estimate the bond angle, θ, of $113^\circ \pm 5^\circ$. A simple self-consistent field *ab initio* calculation using an effective core potential supported the results. The ground state pure rotational spectra of all five isotopologues have been recorded and analyzed[4] from which a bond length, R_{Zr-O}, of 1.7710 ± 0.0007 Å and a O–Zr–O bond angle, θ, of $108.11 \pm 0.08^\circ$ were derived. In that same study the electric dipole moment, μ, was determined to be 7.80 ± 0.02 D and the harmonic bending frequency, ω_2, was estimated as 290 cm^{-1} from the inertial defect. The electronic structure of ZrO_2 was also investigated by photoelectron spectroscopy (PES) of the anion, ZrO_2^-.[5,6] Progressions in the PES spectrum were analyzed to determine symmetric stretching frequency, ω_1, of 887 ± 40 cm^{-1} for the $\tilde{X}^1A_1$ state and an adiabatic electron affinity of 1.64 ± 0.03 eV for the neutral. The 355 nm radiation used was insufficient to probe the regions of low-lying excited states of the neutral. *Ab initio* calculations[6] using a coupled cluster method with single, double, and non-iterative triple excitations (CCSD(T)) were performed in support of the PES results. R_{Zr-O} and θ were predicted to be 1.797 Å and 109.6°, respectively, and ω_1, ω_2, and ω_3 of 887 cm^{-1}, 281 cm^{-1}, and 835 cm^{-1}. In a separate study, high level *ab initio* calculations were performed to model the 355 nm photodetachment spectrum.[7] At the CCSD(T) level, the predicted ω_1, ω_2, and ω_3 for $\tilde{X}^1A_1$ were 909 cm^{-1}, 278 cm^{-1}, and 841 cm^{-1}, respectively. More recently, various high-level *ab initio* and density functional theory (DFT) predicted the properties of the $\tilde{X}^1A_1$ and the low-lying $\tilde{B}^3B_2$ states.[8] The CCSD(T) theory gave R_{Zr-O} and θ values for the $\tilde{X}^1A_1$ which were 1.802 Å and 109.7°, respectively, and the ω_1 and ω_3 of 924 cm^{-1} and 860 cm^{-1}. The splitting between $\tilde{X}^1A_1$ and $\tilde{B}^3B_2$ states varied from 1.82 eV to 2.33 eV depending upon the method employed. The equation-of-motion (EOM) at the

a)Author to whom correspondence should be addressed. Electronic mail: tsteimle@ASU.edu. Tel.: (480) 965-3265.

EOM-CCDS level gave a separation of 2.14 eV. There are no predictions for the $\tilde{A}^1B_2$ state.

Here, we report on the first detection of the electronic transition for ZrO_2. The electronic spectrum has been recorded using laser induced fluorescence (LIF) detection in the region from 17 000 cm^{-1} to 18 800 cm^{-1} and by mass-resolved resonance enhanced multi-photoionization (REMPI) spectroscopy from 17 000 cm^{-1} to 21 000 cm^{-1}. This is a continuation of our studies of Group IVA metal dioxides.[9,10] The electronic spectra are modeled using multi-dimensional Franck-Condon factors (FCFs). An *ab initio* prediction is also performed.

II. EXPERIMENT

The experimental set-ups for the mass selected resonant enhanced multi-photon ionization (MS-REMPI), LIF, dispersed laser induced fluorescence (DLIF), and radiative lifetime measurements were nearly identical to those of the previous study of TiO_2.[9,10] The MS-REMPI measurements were carried out at the University of Basel (UB) using the spectrometer previously described.[11] The LIF, DLIF, and lifetime measurements were performed at the Arizona State University (ASU). In all experiments ZrO_2 was produced by laser ablation of a pure zirconium rod in the presence of a supersonic expanding mixture of ~5% O_2 in either argon (ASU) or helium (UB). The supersonic expansion products were skimmed to produce a well collimated molecular beam. In the low-resolution ($\Delta\nu = \pm 90$ GHz), REMPI experiment ions were removed by applying an electric potential on the skimmer before the molecular beam enters the ionization region of a Wiley–McLaren time-of-flight mass spectrometer.[12] Neutral molecules were irradiated with a pulse of tunable photons from an optical parametric oscillator system (excitation laser) followed by 7.9 eV ($\lambda = 157$ nm) photons from an F_2 excimer laser (ionization laser). Ions were extracted into a time-of-flight tube where the signal from a microchannel plate ion detector was sent to a fast oscilloscope and data acquisition card. The combination of the tunable and 7.9 eV photons was sufficient to ionize ZrO_2, exceeding the ionization potential of 9.4 eV.[13]

In the LIF, DLIF, and lifetime measurements the supersonic free-jet expansion was probed 10 cm from the source with an excimer pumped pulsed dye laser, having a linewidth of ~0.1 cm^{-1}. The laser frequency was calibrated by recording the neon optogalvanic spectrum. In the LIF excitation and radiative lifetime measurements, the fluorescence was viewed off resonance through a 650 nm long-pass filter and was detected with a cooled photomultiplier tube and processed with a box-car integrator. The radiative lifetimes were measured using the same set-up but with the LIF signal recorded on a digital storage oscilloscope. The DLIF spectra were recorded by tuning the wavelength of the pulsed dye laser to excite the most intense feature of each band and viewing the LIF signal through a 2/3 m scanning monochromator. The slit widths were adjusted to produce a spectral linewidth FWHM—of ~20 Å. The signal was detected using a cooled photomultiplier tube and processed using gated photon counting.

III. COMPUTATIONAL DETAILS

Several first-principle computational approaches have been applied to calculate the properties of the $^{90}Zr^{16}O_2$ monomer. For the structural optimization and vibrational frequency calculation of the $\tilde{X}^1A_1$ state, two categories of computations were applied: (1) DFT with the B3LYP functional and (2) complete active space self-consistent field (CASSCF), and CASSCF with the second-order perturbation (CASPT2) for the treatment of dynamical electron correlation. For the two lowest singlet excited states ($\tilde{A}^1B_2$ and $\tilde{B}^1A_1$), time-dependent density functional theory (TD-DFT) and complete active space (CAS) procedures were applied to determine vertical and adiabatic energy gaps and geometries. In the CAS procedures, all valence electrons and orbitals except the innermost ones composed of the O(2*s*) atomic orbitals were selected, forming the (12,12) active space. The Los Alamos effective core potential (ECP) plus double-zeta (LanL2DZ) (Ref. 14) basis set were employed, and the Stevens, Basch, Krauss and Jasien effective core potentials (SBKJ ECP) (Refs. 15 and 16) were also used for comparison.

Systematic scans on the potential energy surfaces (PES) were performed by varying the geometry of the molecule. In the one-dimensional PES scan (cf. Ref. 17), the O–Zr–O bending angle was varied from 40° to 180° by a step of 5°, followed by a partial geometry optimization and excited state calculation at each fixed angle. TD-DFT was applied in these scans to describe up to five singlet excited states. All the DFT and CAS calculations were performed with GAUSSIAN 09 (Ref. 18) and MOLPRO 2006 (Ref. 19) computational packages, respectively.

IV. OBSERVATION

There are five stable isotopes of zirconium: ^{90}Zr(51.5%), ^{91}Zr(11.2%), ^{92}Zr(17.2%), ^{94}Zr(17.4%), and ^{96}Zr(2.8%). The MS-REMPI spectrum of $^{90}ZrO_2$ in the 17 000 cm^{-1}–21 000 cm^{-1} region and the LIF spectrum of the ablation products in the 17 000 cm^{-1}–18 800 cm^{-1} region are presented in Figure 1. Based upon the analogy with TiO_2,[9,10] the spectral simulation, and the *ab initio* prediction (*vide infra*), the spectra are assigned to progressions in the $\tilde{A}^1B_2$ (ν_1, ν_2, ν_3) ← $\tilde{X}^1A_1$ (0, 0, 0) transition. The relative intensities of the bands in the LIF spectrum are nearly identical to those for the MS-REMPI spectrum. The band marked with an "*" in the LIF spectrum is the $C^1\Sigma^+$–$X^1\Sigma^+$(1, 0) transition of ZrO. The $C^1\Sigma^+$–$X^1\Sigma^+$ (0, 0) transition of ZrO overlaps the $\tilde{A}^1B_2$ (0, 0, 0) ← $\tilde{X}^1A_1$ (0, 0, 0) band of ZrO_2. The ZrO spectral features can be suppressed relative to those for ZrO_2 by adjusting the production conditions and by using a long gate time (≈1 μs) on the box car integrator. The lifetime of the $C^1\Sigma^+$–$X^1\Sigma^+$ transition of ZrO is ~130 ns,[20] whereas the lifetimes for the bands of ZrO_2 are much longer (*vide infra*). There are no features to the red of the band at 17 041 cm^{-1}, so it was assigned to the $\tilde{A}^1B_2$ (0, 0, 0) ← $\tilde{X}^1A_1$ (0, 0, 0) transition, assuming adiabatic expansion conditions and that only the $\tilde{X}^1A_1$ (0, 0, 0) level is populated. The assignments, transition wavenumber, difference between the observed transition

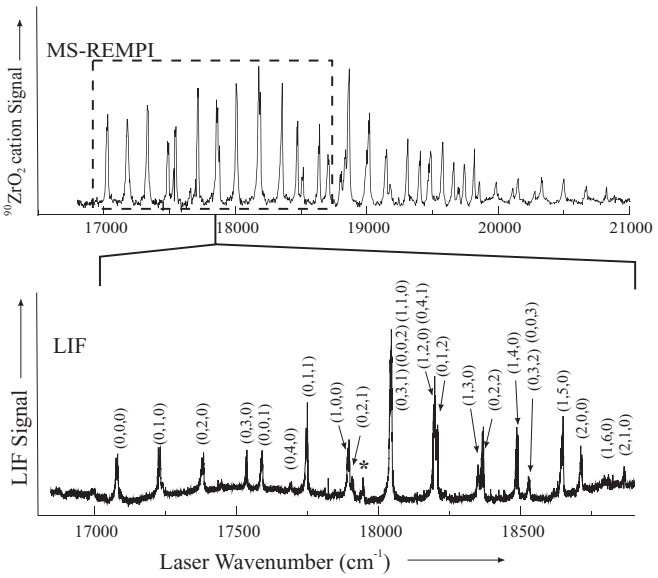

FIG. 1. Mass selected resonance enhanced multiphoton ionization (MS-REMPI) spectrum (top) and laser induced fluorescence (LIF) spectrum (bottom) of $\tilde{A}^1B_2(\nu_1, \nu_2, \nu_3) \leftarrow \tilde{X}^1A_1(0, 0, 0)$ transition of ZrO_2. The spectral feature marked with "*" is the $C^1\Sigma^+ - X^1\Sigma^+(1, 0)$ transition of ZrO. The $C^1\Sigma^+ - X^1\Sigma^+(0, 0)$ transition of ZrO overlaps the $\tilde{A}^1B_2(0, 0, 0) \leftarrow \tilde{X}^1A_1(0, 0, 0)$ band of ZrO_2.

wavenumbers and those calculated using the optimized parameters, and the predicted Franck-Condon factors are given in Table I.

The DLIF spectra resulting from the excitation of the 13 bands observed via LIF were recorded. In all cases no features to the blue of the excitation wavelength were observed, confirming that the lower level associated with the LIF spectra is the $\tilde{X}^1A_1$ (0, 0, 0) state. DLIF spectra resulting from the excitation of the $\tilde{A}^1B_2$ (0, 0, 0) $\leftarrow \tilde{X}^1A_1$ (0, 0, 0) (17 041 cm^{-1}), $\tilde{A}^1B_2$ (0, 0, 1) $\leftarrow \tilde{X}^1A_1$ (0, 0, 0) (17 562 cm^{-1}), and $\tilde{A}^1B_2$ (1, 0, 0) $\leftarrow \tilde{X}^1A_1$ (0, 0, 0) (17 870 cm^{-1}) bands are presented in Figure 2. Similar to TiO_2,[10] long progressions in the bending $\nu_2(a_1)$ mode (e.g., Figure 2(a) $\tilde{A}^1B_2$ (0, 0, 0) $\rightarrow \tilde{X}^1A_1$ (0, ν_2, 0)) and symmetric stretch $\nu_1(a_1)$ mode (e.g., Figure 2(b) $\tilde{A}^1B_2$ (1, 0, 0) $\rightarrow \tilde{X}^1A_1$ (ν_1, 0, 0)) and combinations of $\nu_1(a_1)$ and $\nu_2(a_1)$ modes (e.g., Figure 2(a) $\tilde{A}^1B_2$ (0, 0, 0) $\rightarrow \tilde{X}^1A_1$ (ν_1, ν_2, 0)) are observed. Unlike TiO_2,[10] long progressions in the antisymmetric $\nu_3(b_2)$ mode (e.g., Figure 2(c) $\tilde{A}^1B_2$ (0, 0, 1) $\rightarrow \tilde{X}^1A_1$ (0, 0, ν_3)) and combinations of $\nu_3(b_2)$ and $\nu_2(a_1)$ modes (e.g., Figures 2(b) and 2(c) $\tilde{A}^1B_2$ (0, 0, 1) $\rightarrow \tilde{X}^1A_1$ (0, ν_2, ν_3)) are observed. A total of 268 features for the 13 DLIF spectra were assigned and positions were measured. The transition wavenumber, assignments, and the difference between the observed shifts and those calculated using the optimized parameters are available via the supplementary material or through the author (T.C.S.).[21]

Fluorescence decay curves of the 13 bands observed in the LIF spectrum were recorded. The curves resulting from the excitation of the $\tilde{A}^1B_2$ (0, 0, 0) $\leftarrow \tilde{X}^1A_1$ (0, 0, 0) band at 17 041 cm^{-1} and $\tilde{A}^1B_2$ (0, 0, 1) $\leftarrow \tilde{X}^1A_1$ (0, 0, 0) band at 17 562 cm^{-1} are presented in Figure 3. The curves exhibit single exponential dependence with the $\tilde{A}^1B_2$ (0, 0, 0) lifetime being significantly shorter than that of $\tilde{A}^1B_2$ (0, 0, 1) state.

TABLE I. Observed and calculated band maxima (cm^{-1}) for the $\tilde{A}^1B_2 \leftarrow \tilde{X}^1A_1$ electronic transition of ZrO_2.

Assignment (ν_1, ν_2, ν_3)	Observed (cm^{-1})	Obs.-calc. (cm^{-1})	FCF
(0, 0, 0)	17 041	–9	5.01×10^{-2}
(0, 1, 0)	17 194	–9	1.34×10^{-1}
(0, 2, 0)	17 351	–4	1.28×10^{-1}
(0, 3, 0)	17 506	–1	4.75×10^{-2}
(0, 0, 1)	17 562	8	5.06×10^{-2}
(0, 4, 0)	17 663	4	2.86×10^{-3}
(0, 1, 1)	17 723	12	1.35×10^{-1}
(1, 0, 0)	17 873	4	6.48×10^{-2}
(0, 2, 1)	17 888	20	1.30×10^{-1}
(0, 0, 2)	18 026	–16	4.79×10^{-2}
(0, 3, 1)	18 026	1	1.42×10^{-1}
(1, 1, 0)	18 026	1	1.20×10^{-3}
(1, 2, 0)	18 181	2	2.89×10^{-3}
(0, 4, 1)	18 181	0	1.02×10^{-1}
(0, 1, 2)	18 193	–9	3.19×10^{-3}
(1, 3, 0)	18 336	2	2.02×10^{-2}
(0, 2, 2)	18 357	–7	3.07×10^{-3}
(1, 4, 0)	18 476	–14	1.83×10^{-4}
(0, 0, 3)	18 518	7	1.14×10^{-3}
(0, 3, 2)	18 518	–7	3.63×10^{-3}
(1, 5, 0)	18 643	–2	4.21×10^{-3}
(2, 0, 0)	18 706	18	4.49×10^{-2}
(1, 6, 0)	18 806	6	2.08×10^{-3}
(2, 1, 0)	18 863	17	8.10×10^{-2}
(2, 2, 0)	19 020	16	4.16×10^{-2}
(2, 3, 0)	19 173	11	2.99×10^{-3}
(2, 0, 1)	19 173	–19	4.54×10^{-2}
(2, 4, 0)	19 310	–10	1.88×10^{-3}
(0, 0, 5)	19 404	6	2.17×10^{-4}
(3, 0, 0)	19 484	–23	2.21×10^{-2}
(0, 1, 5)	19 575	3	5.77×10^{-4}
(3, 1, 0)	19 660	–8	3.25×10^{-2}
(2, 0, 2)	19 691	12	1.07×10^{-3}
(0, 2, 5)	19 738	–9	5.55×10^{-4}
(3, 2, 0)	19 816	–12	1.13×10^{-2}
(2, 1, 2)	19 851	5	1.94×10^{-3}
(0, 3, 5)	19 907	–14	2.05×10^{-4}
(3, 3, 0)	19 982	–7	4.19×10^{-5}
(0, 4, 5)	20 107	11	1.24×10^{-5}
(3, 4, 0)	20 147	–3	1.58×10^{-3}
(0, 5, 5)	20 274	4	6.61×10^{-5}
(4, 0, 0)	20 323	–2	8.67×10^{-3}
(4, 1, 0)	20 494	5	1.02×10^{-2}
(4, 2, 0)	20 663	10	2.21×10^{-3}
(4, 3, 0)	20 819	2	9.67×10^{-5}

Std. dev. = 9.64 cm^{-1}

V. ANALYSIS

The observed 268 spectral features in the DLIF (Ref. 21) spectra were fit using the phenomenological expression:[22]

$$G(\nu_1, \nu_2, \nu_3) = T_e + \sum_{i=1\rightarrow 3} \omega_i \left(v_i + \frac{1}{2}\right) + \sum_{i=1\rightarrow 3} \sum_{k=1\rightarrow 3} \chi_{ik} \left(v_i + \frac{1}{2}\right)\left(v_k + \frac{1}{2}\right). \quad (1)$$

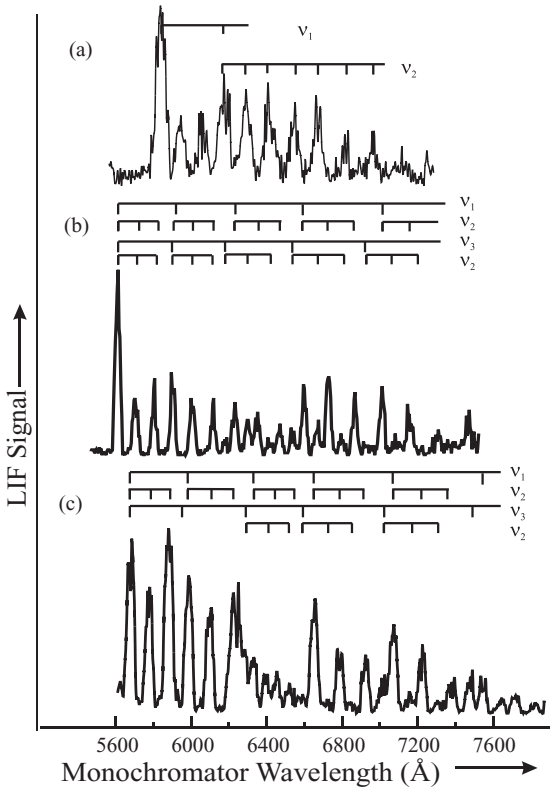

FIG. 2. Dispersed laser induced fluorescence (DLIF) spectra resulting from the excitation of: (a) the $\tilde{A}^1B_2(0, 0, 0) \leftarrow \tilde{X}^1A_1(0, 0, 0)$ band at 17 041 cm^{-1}; (b) the $\tilde{A}^1B_2(0, 0, 1) \leftarrow \tilde{X}^1A_1(0, 0, 0)$ band at 17 562 cm^{-1}; and (c) the $\tilde{A}^1B_2(1, 0, 0) \leftarrow \tilde{X}^1A_1(0, 0, 0)$ band at 17 870 cm^{-1}.

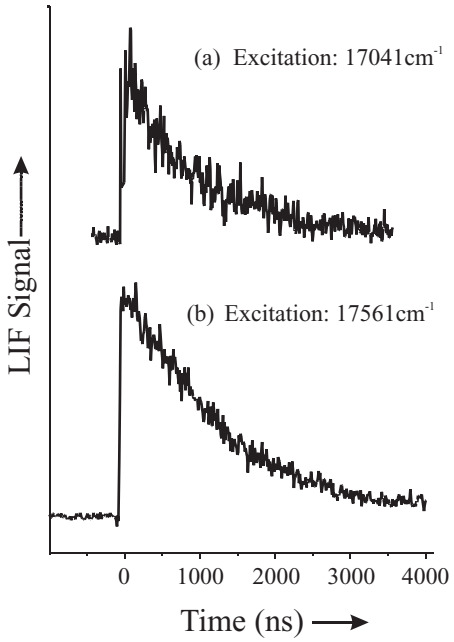

FIG. 3. Fluorescent decay curves resulting from excitation of: (a) the $\tilde{A}^1B_2(0, 0, 0) \leftarrow \tilde{X}^1A_1$ (0, 0, 0) band at 17 041 cm^{-1} and (b) the $\tilde{A}^1B_2(0, 0, 1) \leftarrow \tilde{X}^1A_1(0, 0, 0)$ band at 17 562 cm^{-1}. The radiative lifetime of the $\tilde{A}^1B_2(0, 0, 0)$ state is less than that for the $\tilde{A}^1B_2(0, 0, 1)$.

Various combinations of the anharmonic parameters, χ_{ik}, were attempted. In the end, the DLIF data set could be satisfactorily fit by varying only χ_{22} and χ_{33} in addition to ω_1, ω_2, and ω_3 for the $\tilde{X}^1A_1$ state. The optimized vibrational parameters and their errors are presented in Table II. The standard deviation of the fit ($\sigma = 9.45$ cm^{-1}) is commensurate with estimated measurement uncertainty of the DLIF.

Forty spectral features of the excitation spectra were assigned to 45 transitions and fit using Eq. (1). The 20 LIF features of this data set were assigned a weight three times that of the 20 lower resolution MS-REMPI spectral features. Only the more precisely measured LIF spectral features were included for transitions that were measured both by MS-REMPI and LIF. Various combinations of the anharmonic terms were attempted. In the end, a fit of the excitation spectra was obtained by varying only χ_{12}, χ_{23}, and χ_{33} in addition to ω_1, ω_2, and ω_3 for the $\tilde{A}^1B_2$ state. The standard deviation of the fit ($\sigma = 9.64$ cm^{-1}) is commensurate with estimated combined measurement uncertainty of the LIF and MS-REMPI spectra. The optimized vibrational parameters for the $\tilde{A}^1B_2$ state and associated errors are presented in Table II.

The LIF decay curves were fit using a non-linear least square method to the single exponential decay model:

$$Y = Y_0 + Ae^{\frac{-(t+t_0)}{\tau}}, \quad (2)$$

where t_0 was fixed to a time after the detection system had recovered from the initial laser scatter (typically 20 ns). Decay curves obtained in the absence of molecules were also recorded and subtracted form those recorded in the presence of the molecules to enhance the signal-to-noise. Time greater than 4 μs was neglected because the molecules drift out of the LIF collection region. The determined lifetimes and associated errors are presented in Table III.

VI. DISCUSSION

The determined ω_1 (898 ± 1 cm^{-1}) and ω_3 (808 ± 3 cm^{-1}) values for the $\tilde{X}^1A_1$ state are similar to 884.3 cm^{-1} and 818 cm^{-1} derived from the analysis of the infrared spectrum of a matrix isolated sample[3] and 887 ± 40 cm^{-1} extracted from the PES spectrum.[6] The ω_2 (287 ± 2 cm^{-1}) is also consistent with the 290 cm^{-1} value estimated from the inertial defect.[4] As expected, ω_1 and ω_2 for the $\tilde{X}^1A_1$ state of ZrO_2 are slightly less than ω_1 (968 ± 7 cm^{-1}) and ω_2

TABLE II. Vibrational constants for the ground ($\tilde{X}^1A_1$) and excited ($\tilde{A}^1B_2$) states of ZrO_2.

$\tilde{X}^1A_1$ Parameter	$\tilde{A}^1B_2$ Value (cm^{-1})	Parameter	Value (cm^{-1})
ω_1	898(1)	T_e	16 307(8)
ω_2	287(2)	ω_1	819(3)
ω_2	808(3)	ω_2	149(3)
χ_{33}	9.86(52)	ω_3	518(4)
χ_{22}	3.52(48)	χ_{12}	2(1)
		χ_{23}	4.43(75)
		χ_{33}	–8.50(78)

TABLE III. Florescence lifetimes for the $\tilde{A}^1B_2(\nu_1, \nu_2, \nu_3)$ states of ZrO_2.

Band (cm^{-1})	(ν_1, ν_2, ν_3)	Lifetime τ (μs)
17 034.8	(000)	0.900(32)
17 189.68	(010)	1.212(17)
17 350.8	(020)	1.095(59)
17 506.01	(030)	1.264(25)
17 561	(001)	1.391(28)
17 723.38	(011)	1.378(22)
17 873.16	(001)	1.128(18)
18 025.73	(002)(031)(110)	1.301(18)
18 181.36	(120)(041)	1.387(19)
18 356.55	(022)	1.373(39)
18 476.25	(140)	1.315(26)
18 642.77	(150)	1.227(30)
18 710.05	(200)	0.925(12)

(323 ± 1 cm^{-1}) for the lighter TiO_2.[9,10] A comparison of ω_3 ($\tilde{X}^1A_1$) is not possible because, unlike ZrO_2, transitions involving $\nu_3(b_2)$ were not detected in the DLIF spectrum of TiO_2. The determined ω_1, ω_2, and ω_3 values for the $\tilde{A}^1B_2$ state are 819 ± 3 cm^{-1}, 149 ± 3 cm^{-1}, and 518 ± 4 cm^{-1}, respectively, whereas the corresponding values for TiO_2 are 876 ± 3 cm^{-1}, 184 ± 1 cm^{-1}, and 316 ± 2 cm^{-1}. There is a large reduction in ω_2 and ω_3 upon excitation to the $\tilde{A}^1B_2$ state for both molecules.

The determined harmonic vibrational frequencies (ω_1, ω_2, and ω_3), structure (R and θ), and term energies, T_e, for the $\tilde{X}^1A_1$ and $\tilde{A}^1B_2$ states are compared with predicted values in Table IV. For the $\tilde{X}^1A_1$ state, the computational methods overestimated the Zr–O bond length by up to 0.08 Å, while the O–Zr–O angle is rather insensitive to methodology and consistent with experiment. The vibrational frequencies and permanent dipole moment are slightly overestimated, typical of these calculations.[6,7] Although the term energy of the $\tilde{A}^1B_2$ state is accurately predicted using TD-DFT, the values for ω_2 and ω_3 are in poor agreement with observations. The calculated T_e, ω_1, ω_2, and ω_3 at the CASSCF/LanL2DZ level of theory are also in poor agreement with the experiment. The imaginary vibrational frequency for $\nu_3(b_2)$, predicted by the CASSCF method, implies that the "equilibrium" geometry is located on a potential saddle point. This is probably the top of the barrier of a double-well mode whose potential is distorted by the vibronic coupling with the higher neighboring $\tilde{B}^1A_1$ state.[23,24] The CASSCF/LanL2DZ equilibrium R and θ of 1.884 Å and 96.6° differ significantly from the TD-DFT/LanL2DZ values of 1.843 Å and 101.8°. There is no direct experimental measurement of R and θ for the $\tilde{A}^1B_2$, but the REMPI and LIF excitation spectra could be best modeled using 1.828 Å and 99.0° (*vide infra*), which are near the TD-DFT values.

The TD-DFT one dimension potential energy surfaces for the six lowest electronic states are presented in Figure 4. The potential minima of the ground and the lowest two singlet states occur between 100° and 110°. In contrast to TiO_2,[17] the $\tilde{C}^1A_2$ state of ZrO_2 is located higher than the $\tilde{B}^1A_1$ state at the Franck-Condon point, and the order changes when the angle increases. In the linear configuration, the $\tilde{A}^1B_2$ and $\tilde{C}^1A_2$ states and the $\tilde{B}^1A_1$ and $\tilde{E}^1B_1$ states become degenerate and straddle becomes the non-degenerate $\tilde{D}^1B_2$ state. The energy ordering is that expected for the five Zr^{+2} (4*d*) orbitals ligand-field split into δ, σ, and π-orbitals by the two axial O^- anions.

TABLE IV. Experimental and theoretical properties for $\tilde{X}^1A_1$ and $\tilde{A}^1B_2$ states of ZrO_2.

Method	R_{Zr-O} (Å)	θ_{O-Zr-O} (°)	T_e (cm^{-1})	ω_1 (a_1)	ω_2 (a_1)	ω_3 (b_2)	μ (D)
$\tilde{X}^1A_1$							
Expt.	1.771 ± 0.0007[a]	108.1 ± 0.08[a]		898 ± 1[b]	287 ± 2[b]	808 ± 2[b]	7.80 ± 0.02[a]
B3LYP [c]	1.806	107.2		915	303	870	8.02
B3LYP[d]	1.806	108.0		906	295	854	8.16
CASSCF[c]	1.827	107.7		882	291	835	8.39
CASPT2[c]	1.846	107.7		833	282	802	8.27
CCSD(T)[e]	1.797	109.6		887	281	835	
CCSD(T)[f]	1.7776	108.26		909	278	841	
CCSD(T)[g]	1.802	109.7		924		860	
$\tilde{A}^1B_2$							
Expt.[b]	1.828 [h]	99.0[h]	16307 ± 8	819 ± 3	149 ± 3	518 ± 4	
TD-B3LYP[c]	1.843	101.8	16 753	855	181	420	4.42
TD-B3LYP[d]	1.842	104.0	16 525	839	174	396	4.29
CASSCF[c]	1.884	96.6	12 586	794	182	350*i*	4.32
CASPT2[c]	1.902	97.3	13 733	...	...	...	4.11

[a]Reference 4.
[b]This work.
[c]This work; calculated using the LanL2DZ basis set.
[d]This work; calculated using the SBKJ basis set.
[e]Reference 6.
[f]Reference 7.
[g]Reference 8.
[h]This work; determined from a comparison of the observed and predicted intensities.

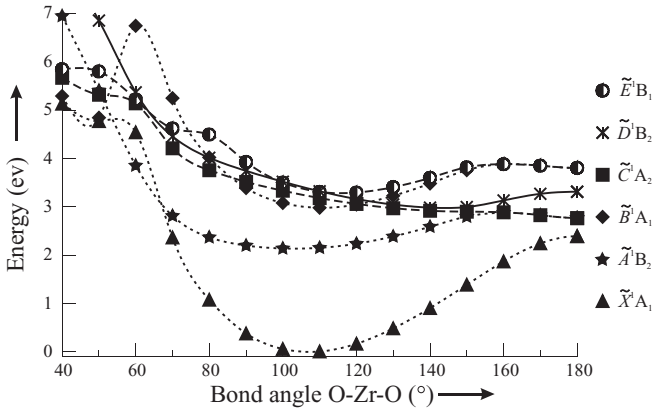

FIG. 4. One-dimensional potential energies for the six lowest electronic states as a function of bending angle obtained using TD-DFT with the B3LYP functional.

Insight into the bonding may be derived from the displacement vectors for the symmetric stretch (Q_1), bend (Q_2), and antisymmetric stretch (Q_3) normal mode motion for the $\tilde{X}^1A_1$ and $\tilde{A}^1B_2$ states shown in Figure 5. The displacement vectors have all been doubled in length for illustrative purposes. The displacement vectors were obtained from a normal mode analysis using the Wilson *GF* matrix approach,[25] details of which are described in Appendix A. The experimental structure of 1.7710 Å and 108.11 ° for the $\tilde{X}^1A_1$ were taken from Ref. 4. The structure for the $\tilde{A}^1B_2$ was taken to be 1.828 Å and 99 ° (*vide infra*). The displacement vectors in Figure 5 describe the motion in $\tilde{X}^1A_1$ and $\tilde{A}^1B_2$ states similar to the ground state of SO_2 which has two strong S–O covalent bonds. In both the $\tilde{X}^1A_1$ and $\tilde{A}^1B_2$ states of ZrO_2, the motion is clearly symmetric Zr–O stretch, O–Zr–O angle bend, and an antisymmetric Zr–O(S–O) stretch as opposed to a Zr–(O_2) stretch, an O–O stretch, and a hindered rotation of the O_2 group against Zr.

The predicted spectra obtained using the methods described below are compared with the observed LIF and REMPI spectra in Figure 6. The observed spectra have not been corrected for the wavelength response of the spectrometers, so only qualitative conclusions can be drawn. The LIF and REMPI excitation spectra were predicted using Eq. (1) to calculate the energies for the $\tilde{X}^1A_1$ and $\tilde{A}^1B_2$ states and FCFs to determine the relative intensities. Details of the FCF prediction are in Appendix B. The FCFs were modeled as the product of the FCF of the two-dimensional problem described by the two a_1-symmetry mode with the FCF for the one-dimensional problem described by the b_2-asymmetry mode:

$$\text{FCF} = |\langle \boldsymbol{\nu'_1 \nu'_2} | \mathbf{00} \rangle|^2 |\langle \boldsymbol{\nu'_3} | \mathbf{0} \rangle|^2. \quad (3)$$

The analytical expressions derived for the one-dimensional case[26] and the two-dimensional case[27] were used. The expressions assume a harmonic potential.[28]

Normally, the strong $\tilde{A}^1B_2$ (ν_1, ν_2, ν_3) ← $\tilde{X}^1A_1$ (0, 0, 0) transitions are via the b_2-component of the electronic transition moment which restricts the transition to even quanta in ν_3. Indeed, implementation of the analytical expression as described in Appendix B predicts no transitions involving odd-ν_3, which is in sharp contrast to the observations (e.g., $\tilde{A}^1B_2$ (0, 0, 1) ← $\tilde{X}^1A_1$ (0, 0, 0) band at 17 562 cm^{-1}). Two approaches can be used to account for the observed odd-ν_3 quanta transitions: (a) allow the displacement of the Q_3 normal coordinate in the Duschinsky transformation (Appendix B) to be non-zero, as done previously for TiO_2;[10] (b) introduce vibronic coupling as done to explain the odd-ν_3 quanta in $\tilde{C}^1B_2$ ← $\tilde{X}^1A_1$ electronic transition of SO_2.[31] The second approach is more realistic and is used here. In this approach the $\tilde{A}^1B_2$ state is assumed to be mixed by vibronic

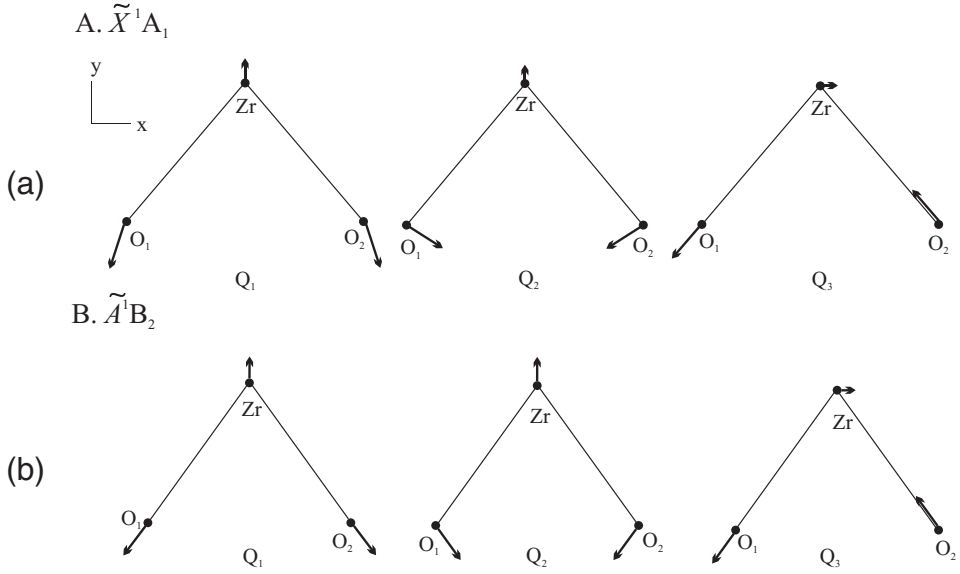

FIG. 5. Displacement vectors for the three vibrational modes of $\tilde{X}^1A_1$ state (a) and $\tilde{A}^1B_2$ state (b) determined using the experimentally derived vibrational frequencies.

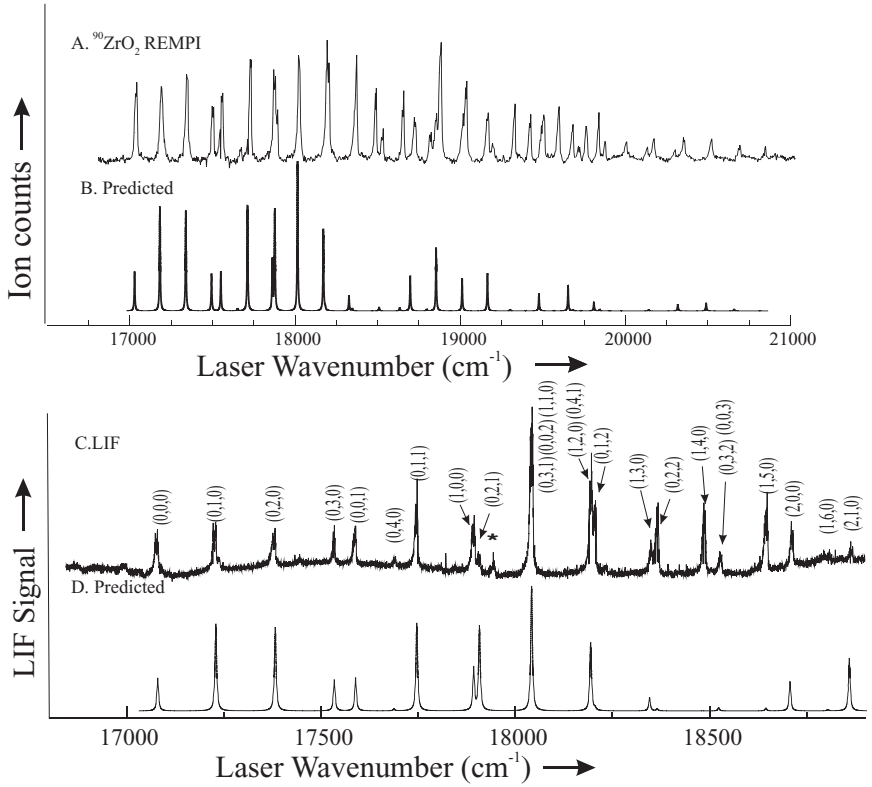

FIG. 6. Top panel: observed (a) and predicted (b) mass selected resonance enhanced multiphoton ionization (MS-REMPI) spectrum in the range of 17 000 cm^{-1}–21 000 cm^{-1} region. Bottom panel: observed (c) and predicted (d) laser induced fluorescence (LIF) spectrum in the range of 17 000–18 000 cm^{-1}. The spectral feature marked with "*" is the $C^1\Sigma^+$–$X^1\Sigma^+(1, 0)$ transition of ZrO.

coupling with the nearby $\tilde{B}^1A_1$ state (see Figure 4). To the first approximation the electronic wavefunction, Φ, becomes

$$\Phi_1(\tilde{A}^1B_2) = \Phi_1^0(\tilde{A}^1B_2) + \frac{\lambda_{21}Q_3}{E(\tilde{A}^1B_2) - E(\tilde{B}^1A_1)}\Phi_2^0(\tilde{B}^1A_1), \tag{4}$$

where

$$\lambda_{21} \equiv \left\langle \Phi_2^0(\tilde{B}^1A_1)\right| (\partial V/\partial Q_3)_0 \left|\Phi_1^0(\tilde{A}^1B_2)\right\rangle. \tag{5}$$

The square of the transition moment then becomes

$$\begin{aligned}&|\langle\Theta_v(\tilde{A}^1B_2)|\langle\Phi_1(\tilde{A}^1B_2)|\mu|\Phi_1(\tilde{X}^1A_1)\rangle|\Theta_v(\tilde{X}^1A_1)\rangle|^2\\ &\quad\approx |\mu_{10}|^2|\langle v_1'v_2'|00\rangle|^2|\langle v_3'|0\rangle|^2\\ &\qquad + c|\mu_{20}|^2|\langle v_1'v_2'|00\rangle|^2|\langle v_3'|1\rangle|^2,\end{aligned} \tag{6}$$

where μ_{10} and μ_{20} are the $\tilde{A}^1B_2 \leftarrow \tilde{X}^1A_1$ and $\tilde{B}^1A_1 \leftarrow \tilde{X}^1A_1$ electronic transition moments, respectively. The first term in Eq. (6) accounts for the transitions involving even quanta in ν_3 and the second involving odd quanta. For the purpose of this prediction it is assumed that $\mu_{10} = \mu_{20}$, which is consistent with TD-DFT results. The coefficient, c, is given by

$$c = \frac{1}{2}\left(\frac{\lambda_{21}}{E(\tilde{A}^1B_2) - E(\tilde{B}^1A_1)}\right)^2. \tag{7}$$

The FCFs were predicted treating c and, as mentioned above, the structure for the $\tilde{A}^1B_2$ state as variables. The optimized value for c, R_{Zr-O}, and θ are 1.1, 1.828 Å, and 99° obtained from a visual comparison of the predicted and observed spectra. Given the TD-DFT/LananL2DZ calculated energies for the $\tilde{A}^1B_2$ (16 753 cm^{-1}) and $\tilde{B}^1A_1$ (23 724 cm^{-1}) states (i.e., $\Delta E = 6970$ cm^{-1}), c corresponds to a vibronic coupling term, λ_{21}, of $\approx 10\,000$ cm^{-1}. A smaller, more realistic, value for λ_{21} would be achieved with a smaller ΔE, allowing μ_{20} to be larger than μ_{10} and/or accounting for interactions with additional states. As expected, the predicted spectrum (Figure 6) is in better agreement with the observation for the low energy portion (i.e., <19 000 cm^{-1}), where vibronic coupling between the $\tilde{A}^1B_2$ and $\tilde{B}^1A_1$ states is expected to be less severe. In general, the relative intensity of combination bands is not predicted as well as overtone bands. For example, the $\tilde{A}^1B_2$ $(1, 4, 0) \leftarrow \tilde{X}^1A_1(0, 0, 0)$ band at 18 476 cm^{-1} and the nearby overlapped $\tilde{A}^1B_2(0, 0, 3) \leftarrow \tilde{X}^1A_1(0, 0, 0)$ and $\tilde{A}^1B_2(0, 3, 2) \leftarrow \tilde{X}^1A_1(0, 0, 0)$ bands at 18 518 cm^{-1}. The intensities of both are underestimated, but the former is predicted to be much less intense than the latter, whereas the opposite is true.

The radiative lifetimes, τ, of ZrO_2 (Table III) are plotted in Figure 7 where it is evident that there are systematic trends as a function of vibrational excitation in the $\tilde{A}^1B_2$ state. Specifically, there is a strong increase in τ in the bending progression with τ $(\tilde{A}^1B_2(0, 0, 0)) = 0.900$ μs and $\tilde{A}^1B_2(0, 3, 0) = 1.264$ μs. One quanta of excitation of ν_3 results in a significant increase in τ: $\tilde{A}^1B_2(0, 0, 1) = 1.391(28)$ μs. The lifetimes decrease for levels that have a

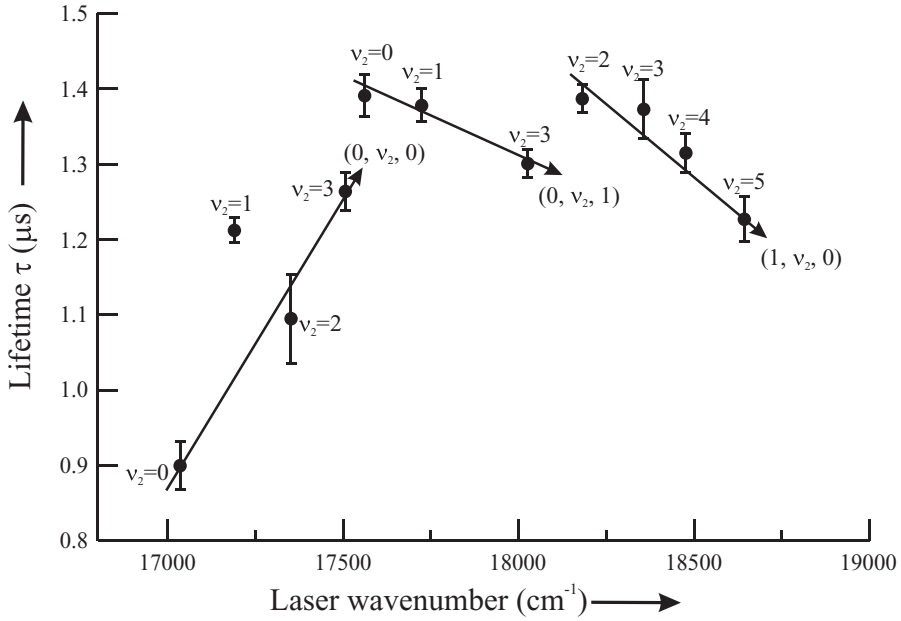

FIG. 7. The trend in fluorescence radiative lifetimes for $\tilde{A}^1B_2(\nu_1, \nu_2, \nu_3) \rightarrow \tilde{X}^1A_1(0, 0, 0)$ transitions of ZrO_2.

combination of one quanta of excitation of either ν_1 or ν_3 and increasing excitation of ν_2. The observed trends are significantly different from those observed for the $\tilde{A}^1B_2$ state of TiO_2 where, for example, the $\tilde{A}^1B_2(0, \nu_2, 0)$ series decrease and the $\tilde{A}^1B_2(1, \nu_2, 0)$ increase with higher bending excitation.

VII. CONCLUSION

Electronic transitions of ZrO_2 in the visible region have been detected and analyzed. The determined vibrational frequencies for the $\tilde{A}^1B_2$ and $\tilde{X}^1A_1$ states demonstrate that there is a significant change in the bonding upon excitation. The dependence of the radiative lifetimes reflects strong vibronic coupling between the $\tilde{A}^1B_2$ and, most likely, the nearby $\tilde{B}^1A_1$ states. The LIF and MS-REMPI excitation spectra could be successfully simulated by including the vibronic coupling. There are similarities between the electronic states of TiO_2, such as a significant decrease in ω_2, a smaller bond angle, and an increase in bond length upon excitation from the $\tilde{X}^1A_1$ to the $\tilde{A}^1B_2$ state. There are also striking differences both in the vibrational dependence of the fluorescence lifetime and the observation of odd-ν_3 quanta transitions in both the excitation and DLIF spectra.

Recording the high resolution LIF spectrum is in progress. The study is more difficult than that for TiO_2 because of the numerous isotopologues, four of which have significant abundances. The analysis will result in a structural determination and confirmation of the vibrational assignment via the inertial defect.[10] The precisely determined vibrational frequencies and term energies determined here will guide future electronic structure calculations.

ACKNOWLEDGMENTS

The work at Arizona State University was supported by grants from the Fundamental Interactions Branch, Division of Chemical Sciences, Office of Basic Energy Sciences, Department of Energy DE-FG02–01ER15153-A003), and that in Basel by the Swiss National Science Foundation (Project No. 200020–124349/1).

APPENDIX A: NORMAL MODE ANALYSIS OF THE $\tilde{X}^1A_1$ AND $\tilde{A}^1B_2$ STATES

The objective is to use experimentally derived information to simulate the LIF and MS-REMPI spectra presented in Figure 1. Evaluation of the analytical expressions used to predict the Franck-Condon factors[29,30] requires relating the normal coordinates of the $\tilde{X}^1A_1$ state, $\mathbf{Q}(\tilde{X}^1A_1)$, to those of the $\tilde{A}^1B_2$ state, $\mathbf{Q}(\tilde{A}^1B_2)$, via the Duschinsky effect:

$$\mathbf{Q}(\tilde{X}^1A_1) = \mathbf{J}\mathbf{Q}(\tilde{A}^1B_2) + \mathbf{D}. \quad \text{(A1)}$$

In Eq. (A1), **D** is the vector of geometry displacements given in terms of the normal coordinates of the ground state ($= \Delta Q_1, \Delta Q_2, \Delta Q_3$) and J is the 3×3 Duschinsky rotation matrix. Both **J** and **D** are obtained from normal coordinate analyses of the $\tilde{X}^1A_1$ and $\tilde{A}^1B_2$ states.

The normal coordinate analyses was performed using the *GF* matrix approach which is well documented by Wilson *et al.*[25] The **B** matrix elements were calculated using the formula in Chapter 2–4 of Ref. 25. The experimental bond length, $R_{Zr–O}$ of 1.7710 ± 0.0007 Å and O–Zr–O bond angle, θ, of $108.11 \pm 0.08^\circ$ for the $\tilde{X}^1A_1$ were taken from Ref. 4. The $R_{Zr–O}$ and θ for the $\tilde{A}^1B_2$ were taken to be 1.828Å and 99° (*vide infra*). The **B** matrices for the $\tilde{X}^1A_1$ and $\tilde{A}^1B_2$

states are

$$\mathbf{B}\left(\tilde{X}^1A_1\right) = \begin{array}{c} \\ \Delta r_1 \\ \Delta r_1 \\ \Delta\theta \end{array} \begin{vmatrix} x_1 & y_1 & z_1 & x_2 & y_2 & z_2 & x_3 & y_3 & z_3 \\ 0 & -0.8096 & 0.5870 & 0 & 0.8096 & -0.5870 & 0 & 0 & 0 \\ 0 & 0.8096 & 0.5870 & 0 & -0.8096 & -0.5870 & 0 & 0 & 0 \\ 0 & 0 & -0.9143\text{Å}^{-1} & 0 & 0.3315\text{Å}^{-1} & 0.4571\text{Å}^{-1} & 0 & -0.3315\text{Å}^{-1} & 0.4571\text{Å}^{-1} \end{vmatrix} \tag{A2}$$

and

$$\mathbf{B}\left(\tilde{A}^1B_2\right) = \begin{array}{c} \\ \Delta r_1 \\ \Delta r_1 \\ \Delta\theta \end{array} \begin{vmatrix} x_1 & y_1 & z_1 & x_2 & y_2 & z_2 & x_3 & y_3 & z_3 \\ 0 & -0.7604 & 0.6494 & 0 & 0.7604 & -0.6494 & 0 & 0 & 0 \\ 0 & 0.7604 & 0.6494 & 0 & -0.7604 & -0.6494 & 0 & 0 & 0 \\ 0 & 0 & -0.8320\text{Å}^{-1} & 0 & 0.3553\text{Å}^{-1} & 0.4160\text{Å}^{-1} & 0 & -0.3553\text{Å}^{-1} & 0.4160\text{Å}^{-1} \end{vmatrix}. \tag{A3}$$

The **G** matrix is related to the **B** matrix by $\mathbf{B}\cdot\mathbf{M}^{-1}\cdot\mathbf{B}^{\mathbf{T}}$, where **M** is the diagonal mass matrix. The **G** matrices for $\tilde{X}^1A_1$ and $\tilde{A}^1B_2$ become

$$\mathbf{G}\left(\tilde{X}^1A_1\right) = \begin{vmatrix} 0.07364\ \text{amu}^{-1} & -0.003457\ \text{amu}^{-1} & -0.005969\ \text{amu}^{-1}\ \text{Å}^{-1} \\ -0.003457\ \text{amu}^{-1} & 0.07364\ \text{amu}^{-1} & -0.005969\ \text{amu}^{-1}\ \text{Å}^{-1} \\ -0.005969\ \text{amu}^{-1}\ \text{Å}^{-1} & -0.005969\ \text{amu}^{-1}\ \text{Å}^{-1} & 04917\ \text{amu}^{-1}\ \text{Å}^{-2} \end{vmatrix} \tag{A4}$$

and

$$\mathbf{G}\left(\tilde{A}^1B_2\right) = \begin{vmatrix} 0.07364\ \text{amu}^{-1} & -0.00174\ \text{amu}^{-1} & -0.006010\ \text{amu}^{-1}\ \text{Å}^{-1} \\ -0.00174\ \text{amu}^{-1} & 0.07364\ \text{amu}^{-1} & -0.006010\ \text{amu}^{-1}\ \text{Å}^{-1} \\ -0.006010\ \text{amu}^{-1}\ \text{Å}^{-1} & -0.006010\ \text{amu}^{-1}\ \text{Å}^{-1} & 0.04512\ \text{amu}^{-1}\ \text{Å}^{-2} \end{vmatrix}. \tag{A5}$$

The three harmonic frequencies for the $\tilde{X}^1A_1$ and $\tilde{A}^1B_2$ states allow for the determination of only three of the four force constants: f_r, f_{rr}, f_θ, and $f_{\theta r}$. In the $\tilde{X}^1A_1$ state, ω_1 (898 cm^{-1}) $\cong \omega_3$ (808 cm^{-1}), so f_{rr} was constrained to zero. A comparison of the eigenvalues of the GF $(\tilde{X}^1A_1)$ with the observed frequencies gives

$$\mathbf{F}\left(\tilde{X}^1A_1\right) = \begin{vmatrix} 4.9863\ \text{mdyn}\,\text{Å}^{-1} & 0 & 1.7797\ \text{mdyn}\,\text{Å}^{-1}\,\text{rad}^{-1} \\ 0 & 4.9863\ \text{mdyn}\,\text{Å}^{-1} & 1.7797\ \text{mdyn}\,\text{Å}^{-1}\,\text{rad}^{-1} \\ 1.7797\ \text{mdyn}\text{Å}^{-1}\,\text{rad}^{-1} & 1.7797\ \text{mdyn}\,\text{Å}^{-1}\,\text{rad}^{-1} & 2.7351\ \text{mdyn}\,\text{Å}^{-2}\,\text{rad}^{-1} \end{vmatrix}. \tag{A6}$$

In the $\tilde{A}^1B_2$ states, ω_1 (819 cm^{-1}) is much greater than ω_3(518 cm^{-1}) and $f_{\theta r}$ was constrained to zero. A comparison of the eigenvalues of the GF $(\tilde{A}^1B_2)$ with the observed frequencies gives

$$\mathbf{F}\left(\tilde{A}^1B_2\right) = \begin{vmatrix} 3.7938\ \text{mdyn}\,\text{Å}^{-1} & 1.6971\ \text{mdyn}\,\text{Å}^{-1} & 0 \\ 1.6971\ \text{mdyn}\,\text{Å}^{-1} & 3.7938\ \text{mdyn}\,\text{Å}^{-1} & 0 \\ 0 & 0 & 0.29667\ \text{mdyn}\,\text{Å}^{-1}\,\text{rad}^{-2} \end{vmatrix}. \tag{A7}$$

The eigenvector matrices, **V**, for the $\tilde{X}^1A_1$ and the $\tilde{A}^1B_2$ states are

$$\mathbf{V}\left(\tilde{X}^1A_1\right) = \begin{vmatrix} & Q_1 & Q_2 & Q_3 \\ \Delta r_1 & -0.6275 & 0.3751 & 0.7071 \\ \Delta r_2 & -0.6275 & 0.3751 & 0.7071 \\ \Delta\theta & 0.4610 & 0.8477 & 0 \end{vmatrix}, \tag{A8}$$

$$\mathbf{V}\left(\tilde{A}^1B_2\right) = \begin{vmatrix} & Q_1 & Q_2 & Q_3 \\ \Delta r_1 & -0.7019 & 0.00467 & 0.7071 \\ \Delta r_2 & -0.7019 & 0.00467 & 0.7071 \\ \Delta\theta & 0.1213 & 0.9999 & 0 \end{vmatrix}. \tag{A9}$$

The internal symmetry coordinates, **S**, are related to the normal coordinates, **Q**, by

$$\mathbf{S} = \mathbf{LQ}, \tag{A10}$$

where **L** and **V** differ only by a normalization constant[29] chosen to assure that $\mathbf{LL}^{\mathrm{T}} = \mathbf{G}$:

$$\mathbf{L} = \mathbf{VN} \tag{A11}$$

with

$$\mathbf{N} = [\mathbf{V}^{-1}\mathbf{G}(\mathbf{V}^{\mathrm{T}})^{-1}]^{1/2}. \tag{A12}$$

The results are

$$\mathbf{L}\left(\tilde{X}^1A_1\right) = \begin{vmatrix} & Q_1 & Q_2 & Q_3 \\ \Delta r_1 & -0.1688 & .08133 & 0.1963 \\ \Delta r_2 & -0.1688 & .08133 & -0.1963 \\ \Delta\theta & 0.1240 & 0.1838 & 0 \end{vmatrix}, \tag{A13}$$

$$\mathbf{L}\left(\tilde{A}^1B_2\right) = \begin{vmatrix} & Q_1 & Q_2 & Q_3 \\ \Delta r_1 & -0.1896 & .00098 & 0.1941 \\ \Delta r_2 & -0.1896 & .00098 & -0.1941 \\ \Delta\theta & 0.03278 & 0.2099 & 0 \end{vmatrix}. \tag{A14}$$

The atomic displacement matrix, **AA**, is calculated by

$$\mathbf{AA} = \mathbf{M}^{-1}\mathbf{B}^{\mathrm{T}}(\mathbf{L}^{-1})^{\mathrm{T}}, \tag{A15}$$

which for the $\tilde{X}^1A_1$ and the $\tilde{A}^1B_2$ states are

$$\mathbf{AA}\left(\tilde{X}^1A_1\right) = \begin{vmatrix} & Q_3 & Q_2 & Q_1 \\ y_{Zr} & 0 & 0 & -0.04586 \\ x_{Zr} & -0.02206 & -0.04932 & 0 \\ z_{Zr} & 0 & 0 & 0 \\ y_{02} & 0.1614 & -0.07218 & 0.1289 \\ x_{02} & 0.06200 & 0.1386 & -0.09346 \\ z_{02} & 0 & 0 & 0 \\ y_{01} & -0.1614 & 0.07218 & 0.1289 \\ x_{01} & 0.06200 & 0.1386 & 0.09346 \\ z_{01} & 0 & 0 & 0 \end{vmatrix} \tag{A16}$$

and

$$\mathbf{AA}\left(\tilde{A}^1B_2\right) = \begin{vmatrix} & Q_3 & Q_2 & Q_1 \\ y_{Zr} & 0 & 0 & -0.04356 \\ x_{Zr} & -0.03811 & -0.03829 & 0 \\ z_{Zr} & 0 & 0 & 0 \\ y_{02} & 0.1253 & -0.1247 & 0.1224 \\ x_{02} & 0.1071 & -0.1076 & -0.1045 \\ z_{02} & 0 & 0 & 0 \\ y_{01} & -0.1253 & -0.1247 & 0.1224 \\ x_{01} & 0.1071 & -0.1076 & 0.1046 \\ z_{01} & 0 & 0 & 0 \end{vmatrix}. \tag{A17}$$

APPENDIX B: FRANCK-CONDON FACTORS

The 3×3 Duschinsky rotation matrix, **J**, is given by[30]

$$\mathbf{J} = (\mathbf{L}(\tilde{A}^1B_2)\mathbf{B}(\tilde{A}^1B_2))\mathbf{M}^{-1}((\mathbf{L}(\tilde{X}^1A_1))^{-1}\mathbf{B}(\tilde{X}^1A_1))^T. \tag{B1}$$

Substitution of Eqs. (A2), (A3), (A12), and (A13) into Eq. (B1) gives the Duschinsky rotation matrix:

$$\mathbf{J} = \begin{vmatrix} 0.9350 & 0.3546 & 0 \\ -0.3546 & 0.9350 & 0 \\ 0 & 0 & 0.9971 \end{vmatrix}. \tag{B2}$$

J is a block diagonal due to the C_{2v} symmetry and the FCF problem separates into a two-dimensional problem for the two a_1 modes and a one-dimensional problem for the b_2 mode. Interestingly, $\mathbf{J}_{33}$ is not unity implying that the ν_3 vibrational mode couples with rotation about the *c*-principal axis, both having b_2 symmetry.[27]

The Duschinsky displacement vector, **D**, is given by[30]

$$\mathbf{D} = (\mathbf{L}(\tilde{A}^1B_2)\mathbf{B}(\tilde{A}^1B_2))^{-1}(\mathbf{R}_{\mathrm{eq}}(\tilde{A}^1B_2) - \mathbf{R}_{\mathrm{eq}}(\tilde{X}^1A_1)), \tag{B3}$$

where $\mathbf{R}_{\mathrm{eq}}$ is the 9×1 vector of equilibrium Cartesian center of mass coordinates. $\mathbf{R}_{\mathrm{eq}}(\tilde{X}^1A_1)$is the obtained experimental structure (1.771 Å and 108.11 °).[4] Initially, $R_{eq}(\tilde{A}^1B_2)$ was obtained from the *ab initio* predicted structure in Table IV (i.e., 1.843 Å and 101.8 °). The structure was varied to reproduce the observed intensities with the final optimized structure being 1.828Å and 99 °. The **D** vector becomes

$$\mathbf{D} = \begin{pmatrix} 0.5185 \\ 0.5535 \\ 0 \end{pmatrix}. \tag{B4}$$

J, **D,** and the experimentally determined harmonic frequencies are used as an input to the analytical expressions for FCFs (Refs. 26 and 27) derived under the assumption that the $\tilde{A}^1B_2$ and $\tilde{X}^1A_1$ state potentials can be modeled as two displaced and distorted harmonic oscillators.

[1] Y. Gong, M. Zhou, and L. Andrews, Chem. Rev. **109**, 6765 (2009).
[2] M. Kaufman, J. Meunter, and W. Klemperer, J. Chem. Phys. **47**, 3365 (1967).
[3] G. V. Chertihin and L. Andrews, J. Phys. Chem. **97**, 6356 (1995).
[4] D. J. Burgh, R. D. Seunram, and W. J. Stevens, J. Phys. Chem. **111**, 3526 (1999).
[5] O. C Thomas, S. Xu, T. P. Lippa, and K. H Bowen, J. Cluster Sci. **10**(4), 525 (1999).
[6] W. Zheng, K. H. Bowen, Jr., J. Li, I. Dąbkowska, and M. Gutowski, J. Phys. Chem. A **109**, 11521 (2005).
[7] D. K. W. Mok, F. Chau, J. M. Dyke, and E. P. F. Lee, Chem. Phys. Lett. **458**, 11 (2008).
[8] S. Li and D. A. Dixon, J. Phys. Chem. A **114**, 2665 (2010).
[9] H. Wang, T. C. Steimle, C. Apetrei, and J. P. Maier, Phys. Chem. Chem. Phys. **11**, 2649 (2009).
[10] X. Zhuang, A. Le, T. C. Steimle, R. Nagarajan, V. Gupta, and J. P. Maier, Phys. Chem. Chem. Phys. **12**, 15018 (2010).
[11] A. E. Boguslavskiy and J. P. Maier, Phys. Chem. Chem. Phys. **9**, 127 (2007).
[12] W. C. Wiley and I. H. McLaren, Rev. Sci. Instrum. **26**, 1150 (1955).
[13] E. Murad and D. L. Hildenbrand, J. Chem. Phys. **63**, 1133 (1975).
[14] P. J. Hay and W. R. Wadt, J. Chem. Phys. **82**, 270 (1985).
[15] W. J. Stevens, H. Basch, and M. Krauss, J. Chem. Phys. **81**, 6026 (1984).
[16] W. J. Stevens, M. Krauss, H. Basch, and P. G. Jasien, Can. J. Chem. **70**, 612 (1992).
[17] F. Grein, J. Chem. Phys. **126**, 034313 (2007).
[18] M. J. Frisch, G. W. Trucks, H. B. Schlegel *et al.*, GAUSSIAN 09, Revision A.02, Gaussian, Inc., Wallingford, CT, 2009.
[19] MOLPRO, a package of *ab initio* programs designed by H.-J. Werner and P. J. Knowles, version 2006.1, R. Lindh, F. R. Manby, M. Schütz *et al.*

[20]B. Simard, S. A. Mitchell, M. R. Humpries, and P. A. Hackett, J. Mol. Spectrosc. **129**, 186 (1988).
[21]See supplementary material at http://dx.doi.org/10.1063/1.3632053 for three pages of observed and calculated levels for $\tilde{X}^1A_1$ ground state of ZrO_2.
[22]G. Herzberg, *Molecular Spectra and Molecular Structure. III. Electronic Spectra and Electronic Structure of Polyatomic Molecules* (Kreiger, Malabar, 1991).
[23]L. Seidner, G. Stock, A. L. Sobolewski, and W. Domcke, J. Chem. Phys. **96**, 5298 (1992).
[24]C.-K. Lin, M.-C. Li, M. Yamaki, M. Hayashi, and S. H. Lin, Phys. Chem. Chem. Phys. **12**, 11432 (2010).
[25]E. B. Wilson, Jr., J. C. Decius, and P. C. Cross, *Molecular Vibrations* (McGraw-Hill, New York, 1955).
[26]J. L. Chang, J. Mol. Spectrosc. **232**, 102 (2005).
[27]J. L. Chang, J. Chem. Phys. **128**, 174111 (2008).
[28]T. E. Sharp and H. M. Rosenstock, J. Chem. Phys. **41**, 3453 (1964).
[29]G. L. Goodman and J. Berkowitz, in *Molecular Ions*, edited by J. Berkowitz and K. O. Groenveld (Plenum, New York, 1983), p. 69.
[30]P. Chen, in *Unimolecular and Bimolecular Reaction Dynamics*, edited by C. Y. Ng, T. Baer, and I. Powis (Wiley, New York, 1994), Vol. 3, p. 372.
[31]P. C. Ray, M. F. Arendt, and L. J. Butler, J. Chem. Phys. **109**, 13 (1998).